A novel design framework of synthetic radial aperture focusing for volumetric transrectal ultrasound imaging

Hyunwoo Song[1], Jeeun Kang [2,*] and Emad M. Boctor[1,2,*]

[1]Department of Computer Science, Whiting School of Engineering, Johns Hopkins University, Baltimore, Maryland 21218, USA
[2]Laboratory for Computational Sensing and Robotics, Whiting School of Engineering, Johns Hopkins University, Baltimore, Maryland 21218, USA
*Corresponding author. E-mail: kangj@jhu.edu (JK), eboctor@jhu.edu (EMB)

Abstract

In this paper, we present a novel design framework of synthetic radial aperture focusing for three-dimensional (3D) transrectal ultrasound imaging (TRUS-rSAF), in which multiple transmittance/reception events at different scanning angles are synthesized to reconstruct a radial plane in the target volume, securing high spatial resolution and texture uniformity. A theory-based design approach has not been available to push the envelope of the 3D rSAF technique. Herein, a closed-form analytical description of the TRUS-rSAF method is presented for the first time, effectively delineating spatial resolution and grating lobe positions in the radial dimension of a TRUS transducer. We demonstrate a solid optimization workflow based on the theoretical foundation to improve its spatiotemporal resolution, grating lobe artifacts, and signal-to-noise ratio. A specific design criterion was considered to outperform a clinical 3D TRUS imaging as a reference (TRUS-REF), where each radial plane is reconstructed with a single transmittance/reception event using a motorized actuator. The optimized TRUS-rSAF method significantly enhanced spatial resolution up to 50% over the TRUS-REF method while providing clinically effective temporal resolution (2–8 volume/sec) with negligible grating lobe artifacts. The results indicate that the proposed design approach would enable a novel TRUS imaging solution in clinics.

Keywords: synthetic aperture focusing, transrectal ultrasound, volumetric imaging, analytical optimization, ultrasound beamforming

1. Introduction

Transrectal ultrasound (TRUS) imaging is an effective clinical tool for cancer localization, biopsy guidance, and post-treatment surveillance (Perrin, 1992; Trabulsi *et al.*, 2010). For several decades, two-dimensional (2D) TRUS imaging using a 1D linear or curved array transducer has been a standard protocol, but it depends highly on the clinician's dexterity and subjective anatomic interpretation. Clinical urology reports the advantages of 3D TRUS imaging, providing comprehensive anatomic context in prostate, renal and pelvic regions (Coleman *et al.*, 2007), in which a 1D linear array is inserted into rectal space through the longitudinal direction. The volumetric scanning is straightforwardly performed. Radio-frequency (RF) channel data for each radial plane is obtained with a single transmittance/reception event and repeats until filling the entire target volume using a motorized actuator (Fenster & Downey, 2000). Each pixel of the radial plane is beamformed using the RF channel data (usually by back-projection method), and then the image envelope is detected to generate a US image plane as a part of the volume. Once the volume is filled with US images at a scanning interval, internal voxels are interpolated to have a fixed unit pixel distance in the volume. Each radial plane has a certain slice thickness given a fixed elevation focusing lens of the 1D linear array, defining radial spatial resolution. However, the radial spatial resolution is degraded as an imaging depth gets deeper due to lower scanline density and broader slice thickness, which is suboptimal to provide clear anatomical infor-mation to clinicians (Bae & Jeong, 2000; Chang & Song, 2011; Bae *et al.*, 2018).

Synthetic aperture focusing (SAF) techniques have been highlighted in the modern US imaging field for decades, which coherently compound time-multiplexed transmittance/reception events over sequential apertures at a specific target pixel to provide higher spatial resolution and enhanced texture uniformity (Bae *et al.*, 2018). Most of the prior arts have focused on developing better imaging quality in the lateral direction (Bae & Jeong, 2000; Jensen *et al.*, 2006; Chang & Song, 2011; Kim *et al.*, 2013). However, there have also been endeavors to effectuate the SAF technique in volumetric US imaging, necessitating a SAF that synthesizes multiple transmittance/reception events in an arbitrary direction (Nikolov & Jensen, 2000; Pedersen *et al.*, 2007a; Kortbek *et al.*, 2008; Andresen *et al.*, 2010, 2011; Bottenus *et al.*, 2016a). Lucas *et al.* presented an extended SAF technique to synthesize multiple cross-sections in different incident angles and positions for higher spatial and contrast resolution (Lucas *et al.*, 2021). However, it requires a sophisticated wobbling scanning in an open imaging access point, which is inapplicable to the TRUS imaging setup. Intravascular US (IVUS) imaging was also tested with the SAF technique applied in the radial direction of the rotating element (synthetic radial aperture focusing; rSAF), hoping to break through the limitation in spatial resolution defined by rotational scanning interval and focusing tightness. Such imaging setup is notably similar to that in the volumetric TRUS imaging. However, a recent investigation by Kang *et al.* concluded that the rSAF tech-

nique is ineffective with the IVUS imaging configuration (Kang *et al.*, 2021). Kim *et al.* recently presented an rSAF-enhanced framework with a customized TRUS transducer (Kim *et al.*, 2019). However, the progress has been stagnant primarily due to the lack of an analytical approach that enables a theoretical optimization of the TRUS imaging framework.

Herein, we demonstrate an analytical description and theory-based optimization workflow of the rSAF technique for volumetric TRUS imaging (rSAF for 3D TRUS imaging; TRUS-rSAF). To the best of our knowledge, we are the very first to present a closed-form analytical description of the TRUS-rSAF imaging (Section 2). In Section 3, critical parameters defined from the analytical solution were optimized to achieve unprecedented spatial resolution. The corresponding change of signal sensitivity and grating lobe artifacts, also affecting overall TRUS imaging quality, were also characterized. In Section 4, we present a practical case study to balance spatial and temporal resolution, grating lobe artifacts, and contrast with a design criterion to outperform a clinical expectation given by a conventional TRUS (TRUS-REF) imaging, which follows the most straightforward volumetric scanning procedure, scanning each radial scanning with a single transmit/receive event pair.

2. Theory and Implementation

In this section, we establish a theoretical model of the TRUS-rSAF method based on two coordinate frames: {sagittal (z), longitudinal (x), frontal (y)} axes to define the global Cartesian coordination of imaging field-of-view (FOV). {axial, lateral, elevation} axes define the local Cartesian coordination relative to the TRUS linear array. Based on the axes, we define the frontal–sagittal plane as a transverse plane, longitudinal–sagittal plane as a sagittal plane, and frontal–longitudinal plane as a frontal plane. The radial axis is global coordination, combining sagittal and frontal axes. The mathematical derivation is established on the global Cartesian coordination system unless mentioned otherwise.

2.1. Field analysis model of TRUS-rSAF imaging

Figure 1 illustrates the 2D model of the TRUS-rSAF method in frontal and sagittal axes (transverse plane) at a specific longitudinal position x_f of the linear TRUS array. Therefore, we omit the x axis in the model for a more straightforward representation. The acoustic source rotates along with the origin with a rotating radius $r = \sqrt{y_0^2 + z_0^2}$. In the figure, the acoustic wave propagates along with a scanning angle $\theta = \sin^{-1}\alpha$ with respect to the sagittal axis. The velocity potential Φ of the monochromatic spherical wave can be expressed at an observation point (y, z) as

$$\Phi_\alpha (y, z, t) = \frac{e^{-j\omega t}}{j\lambda \|R\|_2} \, \Psi_\alpha (y, z), \tag{1}$$

where ω, λ, and Ψ_α represent the angular frequency of the transmitted acoustic wave, wavelength, and transmit beam pattern, respectively. The continuous transmit beam pattern at a depth of R can be expressed as

$$\Psi_\alpha (y, z) = e^{jkR} = e^{jk\sqrt{(y-r\alpha)^2 + (z-r\beta)^2}}, \tag{2}$$

where $k = 2\pi/\lambda$ represents the wavenumber and $\beta = \cos\theta$.

In the defined coordination, the transmit beam is synthesized by compounding multiple acoustic waves propagating with different radial scanning angles by adjusting the synthetic time delays $\tau(\alpha)$ to be coherently focused on a desired focal point in the trans-
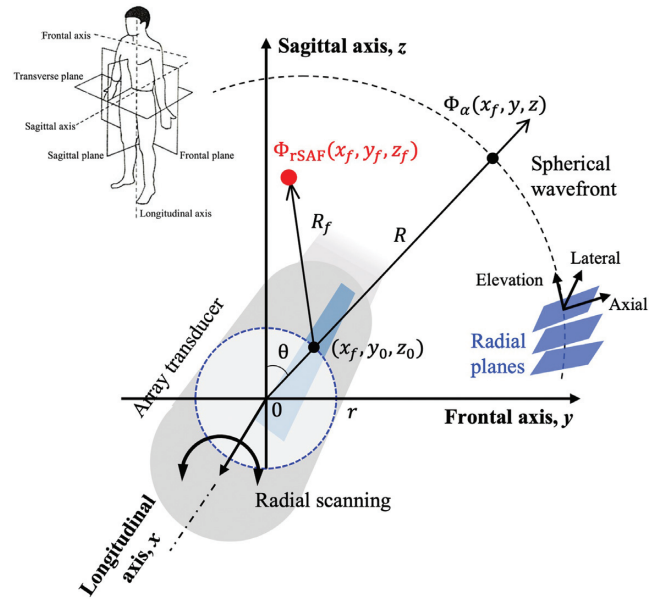

Figure 1: 2D theoretical field analysis model of TRUS-rSAF method in transverse plane (frontal–sagittal axis) at specific longitudinal position $\mathbf{x}_f$. Red dot indicates the synthetic focusing pixel (x_f, y_f, z_f); (x_f, y_0, z_0) is an element position; and θ is a scanning angle in the transverse plane. Left-top image shows the global coordination of the theoretical model.

verse plane at x_f, (y_f, z_f). Thus, the resultant beam pattern can be expressed as

$$\Psi_{\text{rSAF}} (y_f, z_f) = c_0 \int_{-\infty}^{\infty} p_s (\alpha) \, \tau (\alpha) \, \Psi_\alpha (y, z) \, d\alpha, \tag{3}$$

where $c_0 = \frac{1}{j\lambda\|R\|_2}$, $\tau(\alpha)$ represents the synthetic time delay function and $p_s(\alpha)$ denotes the effective radial synthetic window over the range of α used in the TRUS-rSAF imaging. Note that the technological benefit of the TRUS-rSAF method sorely comes from the transmit beam synthesis, while the receive beam pattern will be identical to that of the TRUS-REF method. Therefore, our analytical development will focus on describing the synthesized transmit beam. When the beams are focused at (y_f, z_f) in a specific longitudinal position x_f, the synthetic time delay function is

$$\tau (\alpha) = e^{-jkR_f} = e^{-jk\sqrt{(y_f - r\alpha)^2 + (z_f - r\beta)^2}}. \tag{4}$$

Hence, substituting Equations (2) and (4) to Equation (3) defines the synthetic transmit beam pattern of the TRUS-rSAF imaging as follows:

$$\Psi_{\text{rSAF}} (y_f, z_f) = c_0 \int_{-\infty}^{\infty} p_s (\alpha) \, e^{jk(R - R_f)} d\alpha. \tag{5}$$

By using the Fresnel approximation, $R - R_f$ can be reduced to

$$R - R_f = \frac{y^2 - y_f^2}{2z_f} + \frac{r(y - y_f)}{z_f}\alpha. \tag{6}$$

The Fresnel approximation has been frequently used in the biomedical ultrasound field (Cobbold, 2006) to neglect the non-zero y position of the US element by being considerably smaller than the imaging depth in a target scanline in the axial direction, z_f. Such approximation is usually valid in biomedical ultrasound to image deep tissue with a small US array footprint. Therefore,

substituting Equation (6) with Equation (5) yields the final beam profile:

$$\Psi_{\text{rSAF}}(y_f, z_f) = c_0 e^{jk\frac{y^2-y_f^2}{2z_f}} \int_{-\infty}^{\infty} p_s(\alpha) e^{-jk\frac{r(y-y_f)}{z_f}\alpha} d\alpha$$

$$= c_0 e^{jk\frac{y^2-y_f^2}{2z_f}} \mathcal{F}[p_s(\alpha)]_{f_y=\frac{ry'}{\lambda z_f}}, \qquad (7)$$

where $y' = y - y_f$. In the equation, the synthetic transmit beam pattern is represented by the Fourier transform ($\mathcal{F}[\cdot]$) of the radial synthetic window function $p_s(\alpha)$. When assuming the α range as $[-\alpha_{\max}/2, \alpha_{\max}/2]$ and uniform element directivity in the radial field without apodization, $p_s(\alpha)$, can be expressed as

$$p_s(\alpha) = \text{rect}\left(\frac{\alpha}{\alpha_{\max}}\right). \qquad (8)$$

The resultant synthetic transmit beam pattern of the TRUS-rSAF imaging is acquired by substituting Equation (8) to Equation (7):

$$\Psi_{\text{rSAF}}(y_f, z_f) = c_1 \text{sinc}\left(\frac{r\alpha_{\max}}{\lambda z_f} y'\right), \qquad (9)$$

where $c_1 = c_0 \cdot \alpha_{\max} e^{jk\frac{y^2-y_f^2}{2z_f}}$, and the null-to-null main lobe width (i.e., y'_{ML}) is defined by

$$y'_{\text{ML}} = \frac{\lambda z_f}{r\alpha_{\max}}. \qquad (10)$$

Equation (10) confirms that the spatial resolution of the TRUS-rSAF imaging is proportional to acoustic wavelength (i.e., the fundamental frequency of TRUS transducer) and imaging depth while being inversely proportional to rotation radius r and radial synthetic window defined by $\alpha_{\max}$. The grating lobe is not considered due to a continuous synthetic window $p_s(\alpha)$.

We further practicalized the model using discrete radial scanning angles, as each angle necessitates an individual transmittance/reception event rather than having a continuous aperture in the α domain as in Equation (8). Here, we consider N transmit angles uniformly discretized with an interval $\Delta\alpha$, which can be equated by

$$p'_s(\alpha) = \sum_{n=0}^{N-1} \delta(\alpha - \alpha_n), \qquad (11)$$

where $\alpha_n = \Delta\alpha \cdot n - \alpha_{\max}/2$ and $\Delta\alpha = \alpha_{\max}/(N-1)$. Consequently, the synthetic transmit beam pattern of the TRUS-rSAF imaging can be converted to discretized form as

$$\Psi_{\text{rSAF}}(y_f, z_f) = c_0 e^{jk\frac{y^2-y_f^2}{2z_f}} \sum_{n=0}^{N-1} e^{-jk\frac{r\alpha_n}{z_f}y} = c'_1 \frac{\sin\pi\frac{rN\Delta\alpha}{\lambda z_f}y}{\sin\pi\frac{r\Delta\alpha}{\lambda z_f}y}, \qquad (12)$$

where $c'_1 = c_0 \cdot e^{jk\frac{y^2-y_f^2+r\alpha_{\max}}{2z_f}y}$. The null-to-null main lobe width is given from (12):

$$y'_{\text{S}_{\text{ML}}} = \frac{\lambda z_f}{rN\Delta\alpha} = \frac{\lambda z_f}{r\alpha_{\max}}. \qquad (13\text{-}1)$$

The discretized sampling in α domain results in grating lobes in the beam field positioned at

$$y'_{\text{S}_{\text{GL}}} = \frac{\lambda z_f}{r\Delta\alpha} n \ (n = 1, 2, 3, \ldots). \qquad (13\text{-}2)$$
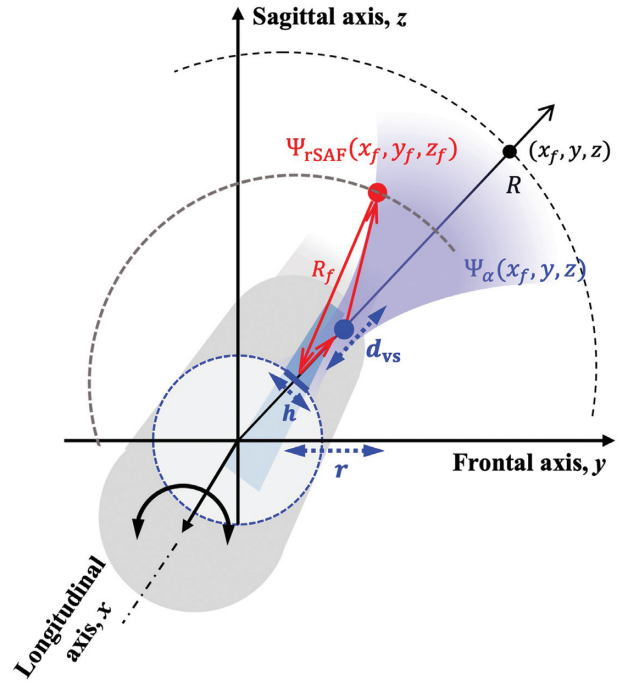

Figure 2: Optimization of TRUS-rSAF method in 2D transverse plane at a specific longitudinal position $\mathbf{x}_f$. Blue indicators show the variables in our rSAF optimization. Red arrows indicate the synthetic time delay $\tau(\alpha)$ of the given radial transmit beam $\Psi_\alpha(y, z)$ to reconstruct the target focusing point (y_f, z_f).

Therefore, our analytical solution of the TRUS-rSAF imaging unveiled that the most critical yet flexible parameters are r and $\Delta\alpha$, defining theoretical spatial resolution and grating lobe positions. We will perform a heuristic optimization on those critical parameters in the following Section 3. For λ, we will follow the well-established specification in the TRUS-REF imaging.

2.2. Implementation using virtual sources

We implement the TRUS-rSAF model synthesizing radial wavefronts diverging from virtual sources (VSs) at a fixed lens focusing point of each radial plane at a specific axial distance d_{VS}. This approach resembles the concept that has been used for the SAF technique in the lateral direction with electrical focusing (Frazier & O'Brien, 1998). Figure 2 defines the revised model of the TRUS-rSAF method. At the VS of each radial plane, the acoustic wavefront forms two-way focusing for transmission and reception, while other depth regions will have a spherical wavefront. The wavefront from each VS can be synthesized by adjusting the time-of-flight passing through the corresponding VS to the target pixel (y_f, z_f) in the transverse plane at a specific longitudinal position x_f. Here, the primary consideration for the SAF with a 1D element should be to count only the transmittance planes providing adequate overlap at the target focal point (Pedersen *et al.*, 2007a; Bottenus *et al.*, 2016a). In synthetic focusing of each radial plane, the radial acoustic wavefront first travels from (y_0, z_0) to the VS with the distance of d_{VS}. From the VS, the acoustic wavefront travels to the focusing point (y_f, z_f), and we denoted this distance as $d_{tf}(i, z)$ at the ith dataset within the synthetic window. Therefore, the distance in the total transmittance pathway is $d_t(i, z) = d_{\text{VS}} + d_{tf}(i, z)$, which results in a transmit time-of-flight, $\tau_t(i, z) = d_t(i, z)/c$, where c is a constant speed of sound in biological tissue (i.e., 1540 m/sec). On the other hand, an acoustic reception distance d_r is defined as the shortest pathway revers-

ing from (y_f, z_f) to element in the TRUS transducer (y_0, z_0), leading to receiving time-of-flight $\tau_r(z) = d_r(z)/c$ (i.e., R_f). In all, adjacent radial planes can be synthesized to the target pixel (y_f, z_f) by compensating the focusing delay at each synthetic angle, $\tau_f(i, z) = \tau_t(i, z) + \tau_r(z)$. The coherent synthesis of effective radial planes in a target imaging slice can be equated by

$$I_{rSAF}(\theta_n, z) = \frac{1}{N_{syn}(z)} \sum_{i=n-N_{syn}(\theta_n, z)/2+1}^{n+N_{syn}(\theta_n, z)/2} \bar{I}_i(\theta_n, z), \quad (14)$$

where $I_{rSAF}(\theta_n, z)$ is a signal intensity in a target radial plane at θ_n, and z of imaging angle and depth, respectively; $N_{syn}(\theta_n, z)$ is the number of effective radial planes for the TRUS-rSAF imaging, defined at specific target radial angle θ_n and imaging depth z by their overlap of adjacent beam profiles; and $\bar{I}_i(\theta_n, z)$ is the US intensity at the focal point (θ_n, z) from ith dataset within the synthetic window which is delay-compensated by $\tau_f(i, z)$. The model is valid for each imaging angle θ_n ($n = 1, 2, ..., N$), comprising entire imaging volume in an interval of $\Delta\theta$ (i.e., $\Delta\theta = \sin^{-1}\Delta\alpha$).

3. Simulation and Optimization

3.1. Spatial resolution-oriented optimization strategy

Equation (13-1) suggests the critical parameters to define the spatial resolution of the TRUS-rSAF imaging: acoustic wavelength λ, radial synthetic window defined by α_{max}, and probe radius r. In practice, the element height h and d_{VS} determines α_{max}, and r determines the overlap among adjacent radial planes. Here, we define the optimal TRUS transducer for the effective rSAF technique with a specific design objective to maximize the spatial resolution (Fig. 2). A heuristic optimization was performed on the critical parameters. Basic design specifications followed those of a clinical TRUS transducer (linear array in BPL9-5/55, BK Ultrasound, Inc.): 6.5 MHz, center frequency; fractional bandwidth, 80%; 5 mm, elevation aperture size h; 20 mm, elevation focusing depth d_{VS}; 10 mm, probe radius r. Imaging parameters were as follows: 0.4724°, rotation interval in degree $\Delta\theta$; 128 or 280 radial scanlines to compose the radial FOVs of [−30°, 30°] and [−66.14°, 66.14°], respectively. The target imaging depth of interest was from 0 to 70 mm. We choose $\Delta\theta$ to scan the deep tissue region at a good interval. Our $\Delta\theta$ at 0.4724° is designed to have 14 scanlines in a single radial full width at half-maximum (FWHM) at deep imaging depth (6.43 mm at 70 mm depth, Fig. 6e) while providing clinically relevant temporal resolution (~6 volume/sec, Fig. 6g). During the optimization, clinically relevant ranges for the critical parameters were evaluated to secure their practicality in clinics: $d_{VS} = \{5, 10, 15, 20, 25\}$ mm; $h = \{3, 4, 5, 6, 7\}$ mm; and $r = \{5, 10, 15\}$ mm. The optimal d_{VS} was first defined for subsequent evaluation of h and r. Note that sound propagation speed c was fixed at 1540 m/s during the optimization.

$N_{syn}(\theta_n, z)$ was determined for each combination of critical parameters to maximize an effective overlap among adjacent beam profiles along the volumetric scanning trajectory in the radial direction. This approach enables us to find the peak spatial resolution by synthesizing only the effective radial transmission/reception events for a target focal point. Using Field-II simulation of wire targets (WTs) in an imaging depth range from 10 to 70 mm at 10 mm intervals, we tested each combinational setup while increasing N_{syn} (i.e., 3, 5, 7, …) until finding the narrowest radial FWHM at a depth of interest (Jensen & Svendsen, 1992; Jensen, 1996). A geometrical beam profile model was configured using h, z_{VS}, and N_{syn} was derived at the deepest imag-

ing depth, 70 mm (i.e., $\overline{N_{syn}}$). The model finally defined $N_{syn}(\theta_n, z)$, giving the corresponding optimal α_{max} at individual depths z [i.e., $\alpha_{max}(z) = \Delta\alpha \cdot N_{syn}(\theta_n, z)$]. The FWHM at each depth was evaluated.

We also evaluated the impact of spatial resolution-oriented optimization on the signal-to-noise ratio (SNR) in the canonical definition:

$$SNR = 20\log_{10} \frac{E\left[I^2(\theta_n, z)\right]}{\sigma^2}, \quad (15)$$

where $E[\cdot]$ is the expectation of the signal amplitude, and σ is the noise power. The definition delivers acoustic power difference between signal and background noise power during data acquisition. A short d_{VS} may secure high α_{max} but result in lower acoustic power density in deep tissue than the clinical TRUS-REF imaging, which deteriorates resultant signal sensitivity. On the other hand, the coherent frame compounding in the TRUS-rSAF framework will bring a counter effect enhancing the signal-to-noise amplitude ratio theoretically with a factor of $\sqrt{N_{syn}(\theta_n, z)}$ if approximating that $I_i(\theta_n, z) = \bar{I}_i(\theta_n, z)$ as in Equation (14). The SNR presents the projected signal sensitivity due to these opposing effects.

The SNR at each combinational parameter setup was evaluated in Field-II imaging simulation. A transmit beam profile was first analyzed in each setup to quantify the acoustic energy over imaging depth. We also simulated WTs located at 10 mm intervals from 10 to 70 mm to define the signal component. In addition, a randomized Gaussian noise image at −20 dB mean intensity was separately simulated in the corresponding imaging FOV to define the noise component. The SNR deviation due to the optimized TRUS-rSAF method was calculated compared to its negative control, named TRUS-CON method here, where imaging is performed with exact specifications as in the optimized TRUS-rSAF method but comprising a target volume with only the center radial plane at each scanning angle. This setup is to omit the benefit of the coherent radial synthesis intentionally. The TRUS-REF method uses a clinical TRUS array transducer (BPL9-5/55 in this study) to represent a clinical performance expected in modern clinics.

Contrast and information entropy contrast (IEC) were measured in the tissue-mimicking Field-II simulation data to compare the TRUS-REF and TRUS-rSAF imaging performance. Contrast represents deviation between hyperechoic and cyst regions and IEC evaluates spatial acuity quantified by microstructural entropy (Hu et al., 2008; Lee et al., 2012; Ju et al., 2015; Tsui et al., 2017), which are defined as

$$Contrast = 10 \log_{10} \frac{\sum_{y,z \subseteq HR} I^2(y, z)}{\sum_{y,z \subseteq CR} I^2(y, z)}, \quad (16)$$

$$IEC = \hat{C} \, InEn, \quad (17)$$

where HR and CR are hyperechoic mass and anechoic cyst regions, respectively. InEn and $\hat{C}$ are an information entropy and a mean contrast, respectively, within the regions-of-interest (ROIs), which are defined by

$$InEn = - \sum_{i=\hat{I}_{min}}^{\hat{I}_{max}} Prob\left(\hat{I}_i\right) \cdot \log_2 \left[Prob\left(\hat{I}_i\right)\right], \quad (17\text{-}1)$$

$$\hat{C} = \frac{1}{(K_y - 1)(K_z - 1)} \sum_{y=0}^{K_y-2} \sum_{z=0}^{K_z-2} |pxl(y, z) - pxl(y, z+1)|, \quad (17\text{-}2)$$

where, $\hat{I}_{min}$ and $\hat{I}_{max}$ are the minimum and maximum grayscale pixel intensities, $Prob(\hat{I}_i)$ is the probability of pixel distribution at ith gray level, and $pxl(y, z)$ is the pixel intensity at (y, z) coordinate (i.e., frontal and sagittal axes, respectively). Contrast is a practical image quality metric that contains multifactor influences dur-

ing image acquisition and reconstruction, including the acoustic power, side lobe artifacts, and grating lobe artifacts at a target ROI.

3.2. Critical parameters in TRUS-rSAF transducer optimization

3.2.1. Impact of d_{VS}

The transmit beam profile of the TRUS array was first analyzed as a function of d_{VS}. 1D radial intensity profiles were extracted at {30, 50, 70} mm using the Field-II simulation of transmit beam pattern (Fig. 3a). The transmit beam profiles become weaker as d_{VS} gets shorter, sacrificing the signal sensitivity at a deep depth. For example, d_{VS} = {5, 10, 15, 20} mm provided {92.75, 79.68, 47.24, 13.50}% and {90.25, 76.40, 62.84, 29.69}% of reductions of maximal acoustic power reaching to at 30 and 70 mm depths, respectively, when compared to the case with d_{VS} at 25 mm (Fig. 3b). Such changes will affect the signal component for SNR calculation. On the other hand, a transmit beam profile had wider beam distribution when the shorter d_{VS} was applied, which resulted in a greater $\overline{N_{syn}}$: {49, 23, 11, 7, 5} (i.e., θ_{max} = {22.67°, 10.39°, 4.72°, 2.83°, 1.89°}) when d_{VS} = {5, 10, 15, 20, 25} mm, respectively. Therefore, a net SNR will be determined by a competing effect of transmit power and synthetic window width specified by d_{VS}, as shown in Fig. 3c. Figure 3d shows the 2D TRUS-rSAF images reconstructed in the transverse plane. The TRUS-rSAF imaging enhanced spatial details in the visual assessment when the shorter d_{VS} was applied. The FWHM measurement at each depth quantitatively validated the trend (Fig. 3e). For example, at 70 mm depth, the FWHM of the target was {3.66, 5.66, 6.37, 6.66, 9.10} mm at d_{VS} = {5, 10, 15, 20, 25} mm, respectively.

It should be noted that the SNR definition in Equation (15) requires equal attention to noise components, which should be related to the coherent compounding effect with $N_{syn}(\theta_n, z)$. Figure 3f shows the SNR difference between the TRUS-CON and TRUS-rSAF imaging with different d_{VS}. It was notable that more significant SNR improvements were obtained in the TRUS-rSAF imaging at deeper imaging depth with shorter d_{VS}. For example, {6.28, 17.13, 22.66, 26.60} dB higher SNRs were achieved at {10, 30, 50, 70} mm depths when d_{VS} = 5 mm, whereas there were only {9.14, 8.01, 11.58, 11.80} dB improvements when d_{VS} = 25 mm.

Note that there was no further analysis on the grating lobe with d_{VS} because no impact is expected given with Equation (13-2).

3.2.2. Impact of h

Figure 4a shows the transmit beam profiles at different h = {3, 4, 5, 6, 7} mm. Note that the d_{VS} is fixed at 5 mm based on the previous optimization, and other parameters were used as given in the clinical reference TRUS transducer. For a fair comparison, we did not equalize the total transmit acoustic power for different h. The acoustic power when h = {4, 5, 6, 7} mm was reduced by {12.64, 21.51, 24.24, 30.74}%, {6.95, 14.65, 16.21, 23.37}%, and {0.61, 3.03, 12.73, 16.97}% at 30, 50, and 70 mm depths, respectively, when compared to the corresponding cases of having h = 3 mm (Fig. 4b). Notably, the intensity changes among h = {4, 5, 6, 7} mm were not simply inversely proportional given by the dependency on the different transmit aperture sizes (Fig. 4c). A net SNR at each depth will be determined by combining the transmit power and $N_{syn}(\theta_n, z)$. One might expect an increase in signal sensitivity proportional to h, giving a wider aperture to detect acoustic signals. However, h is a dominant factor to define the transmit beam divergence from the VS, and more divergency with wider h will lower the sensitivity in the out-of-VS depth range.

The spatial resolution was evaluated for the corresponding setups using the Field-II simulation data of WTs (Fig. 4d). The $\overline{N_{syn}}$ was proportional to h: {23, 37, 51, 61, 65} for h = {3, 4, 5, 6, 7} mm, which was predictable with the divergence of focused wavefront proportional to the transmit aperture width (Fig. 4b). The FWHMs measured at each depth indicated the inversely proportional relationship between FWHM and h (Fig. 4e). For example, the FWHMs of the target at 30 mm are {2.92, 2.50, 2.17, 1.68, 1.48} mm for h = {3, 4, 5, 6, 7} mm, respectively. At 70 mm depth, the FWHMs became {7.76, 4.61, 3.77, 3.66, 3.92} mm for h = {3, 4, 5, 6, 7} mm, respectively. Therefore, the larger h will provide a more consistent and higher spatial resolution.

Figure 4f shows the SNR of the TRUS-CON and TRUS-rSAF imaging with different h. The higher SNRs were obtained when applied the TRUS-rSAF imaging with wider h. Representatively, {5.104, 16.12, 21.59, 25.26} dB higher SNRs were achieved at {10, 30, 50, 70} mm depths when h = 7 mm, whereas there were only {10.73, 12.84, 16.95, 18.95} dB improvements when h = 3 mm. Therefore, the change in h affects SNR by the acoustic divergence and total acoustic power transmittance.

There was no further analysis on the grating lobe with h as no impact is expected with Equation (13-2).

3.2.3. Impact of r

Our analytical solution unveiled that r is the most critical parameter affecting spatial resolution and grating lobe positions. We performed a heuristic optimization by testing a range of r: {5, 10, 15} mm (Fig. 5a). As predicted in Equation (13), the measured FWHMs of the WT at each depth presented the inversely proportional relationship between FWHM and r as shown in Fig. 5c. FWHMs at 30, 50, and 70 mm depths indicated {2.94, 2.34, 2.01} mm, {3.81, 3.16, 2.64} mm, and {5.63, 3.66, 3.38} mm when r is {5, 10, 15} mm, respectively. It can be explained by an interesting observation that the $\overline{N_{syn}}$ is inversely proportional to r when fixed $\Delta\theta$ at 0.4724°: {53, 49, 45} for r = {5, 10, 15} mm, leading to the corresponding radial aperture sizes at {2.18, 4.04, 5.57} mm, respectively (Fig. 5b).

SNR was also calculated at each r. Note that r will not affect the individual radial plane, so the SNR improvements should be determined by $N_{syn}(\theta_n, z)$. Figure 5d presents the SNR proportional to $\overline{N_{syn}}$. For example, 28.39, 26.87, and 26.26 dB SNR improvements were obtained at 70 mm depth when r at {5, 10, 15} mm, respectively.

We consider another crucial impact of r on the positions of grating lobes. The proximity of the first grating lobes to the main lobe at the imaging axis is regarded as inversely proportional to the imaging contrast. Our analytic solution in Equation (13-2) suggests that the enlarged r shifts the grating lobes toward the main lobe. B-mode images with extended dynamic range (Fig. 5e) validate the theoretical expectation matched with theoretical synthetic transmit beam patterns in Fig. 5f. The theoretical first grating lobe positions when r = {5, 10, 15} mm were at ±{43.78, 25.63, 15.99}°, ±{64.03, 50.11, 38.62}°, ±{66.97, 55.19, 44.88}°, and ±{68.10, 57.30, 47.67}° at 10, 30, 50, and 70 mm depths, respectively. The spatial sampling at the VS depth can also explain these results. The sampling intervals in the wavelength unit are {0.35, 0.52, 0.69} λ when r = {5, 10, 15}, which confirms coarser sampling with larger r, bringing more grating lobe artifacts into a scanning angle. Therefore, the TRUS-rSAF imaging with a larger r results in more grating lobe artifacts. The following section of practical optimization will include the strategy to suppress the grating lobe artifacts.
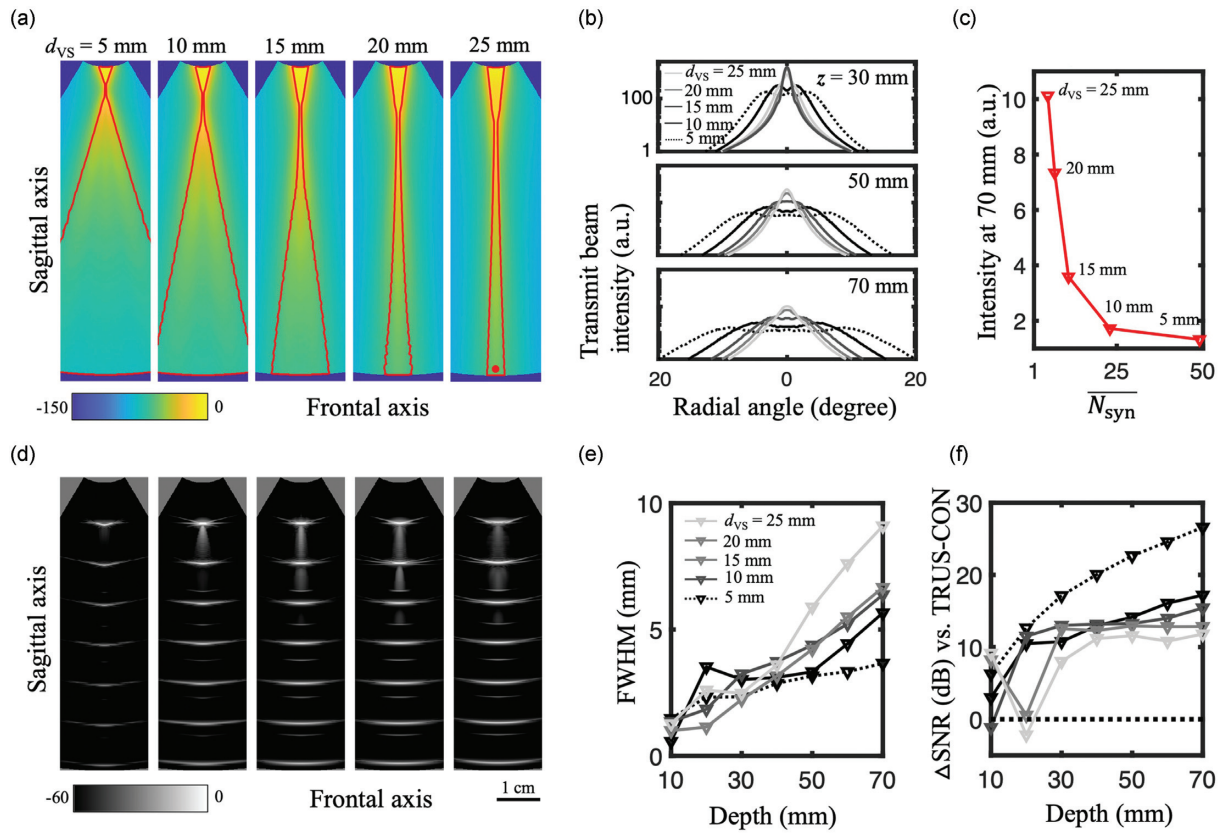
Figure 3: Critical parameter optimization on d_{VS} impact on TRUS-rSAF imaging performance. (a) Transmit beam profiles at different d_{VS}. Red lines indicate −6 dB contour from each depth. Intensity was normalized to the maximum when d_{VS} = 25 mm. (b) Transmit beam intensity at 30, 50, and 70 mm depths. (c) Beam intensity as a function of $\overline{N_{syn}}$ at different d_{VS} on the red observation point in (a). (d) Field-II wire-target simulation data at different d_{VS}. (e) FWHM over imaging depth. (f) SNR difference between the TRUS-rSAF and TRUS-CON imaging over imaging depth.

4. Practical Implementation

In previous sections, we established the analytical approach to design the critical parameters for a TRUS transducer enabling the effective volumetric rSAF technique: d_{VS} = 5 mm, h = 7 mm, and r = 15 mm. This section presents an integrative optimization workflow of the TRUS-rSAF imaging with a specific design criterion to outperform the TRUS-REF imaging that illustrates a basic expectation in clinics.

Figure 6e shows the TRUS-rSAF imaging with the optimal $\overline{N_{syn}}$ at 65 resulting in the {46.67, −11.15, 15.65, 46.75, 54.85, 52.79, 51.00}% narrower FWHMs at {10, 20, 30, 40, 50, 60, 70} mm depths compared to those by the TRUS-REF imaging. To validate the clinical efficacy of the volumetric TRUS-rSAF imaging, we compared the resultant radial imaging resolution at each depth with those by the TRUS imaging using an in-plane micro-convex array (BPC8-4/10) located perpendicular to the linear array for volumetric imaging in our clinical bi-planar TRUS transducer. The specifications of the BPC8-4/10 are as follows: the number of channels, 128; 6 MHz, center frequency; fractional bandwidth, 60%; element pitch, 0.21 mm; element height, 7 mm; the radius of curvature, 10 mm; and f-number in the transmit aperture, 3. Encouragingly, the TRUS-rSAF imaging provided the spatial resolution even higher than the in-plane micro-convex TRUS imaging, as shown in Fig. 6e: {53.26, −1.08, 4.92, 23.93, 34.64, 29.31, 24.78}% narrower FWHMs at {10, 20, 30, 40, 50, 60, 70} mm depths. Detailed simulation setup and results can be found in the Supplementary Information. However, given the current imaging configuration (i.e.,

$\Delta\theta$ = 0.4724°), the TRUS-rSAF image presented noticeable grating lobe artifacts due to coarse radial sampling (Fig. 5a). In addition, low SNR at deep imaging depths, primarily due to the diverging beam field designed to secure the wider synthetic window, should also be addressed. Our analytical description of the TRUS-rSAF method (Equation 13) allows the further optimization of the grating lobe positions and $\overline{N_{syn}}$, while preserving α_{max} to secure the highest spatial resolution. The corresponding change in volume scanning rate will also be analyzed.

4.1. Grating lobe

Figure 6a shows the grating lobe positions in the optimized TRUS-rSAF imaging at $\Delta\theta$ = 0.4724°/{1.00, 1.25, 1.50, 1.75, 2.00, 3.02} (i.e., {0.4724°, 0.3779°, 0.3149°, 0.2699°, 0.2362°, 0.1564°, respectively}). We identified that the original $\Delta\theta$ at 0.4724° presented significant grating lobe artifacts, but its positions shifted far from the target with the finer $\Delta\theta$. Red dots indicate the theoretical grating lobe positions at each target depth, as illustrated in Equation (13-2), and they were well matched with the radial profiles of the WT signal, as shown in Fig. 6c. Therefore, the results validate our analytical approach as a theoretical foundation to design an effective $\Delta\theta$ control to alleviate the grating lobe artifacts.

We herein set our performance benchmark by designing the first grating lobe positions out of the −20 dB radial beam profile of the outmost transverse plane in the synthetic window, by which the grating lobe artifacts can be effectively rejected (TRUS-GLR, Fig. 6b). We set a strict design criterion to reject the grating
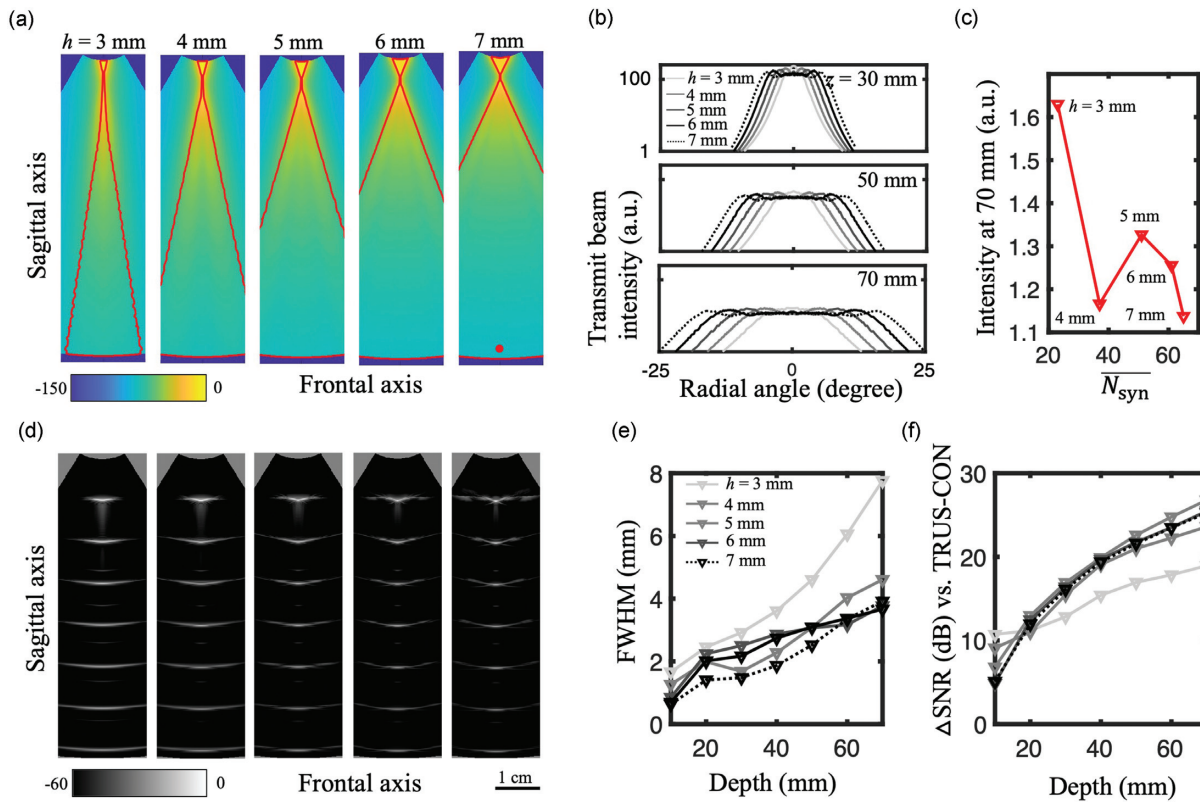
Figure 4: Critical parameter optimization on *h* impact on TRUS-rSAF imaging performance. (a) Transmit beam profiles at different *h*. Red lines indicate −6 dB contour from each depth. Intensity was normalized to the maximum when *h* = 3 mm. (b) Transmit beam intensity at 30, 50, and 70 mm depths. (c) Beam intensity as a function of $\overline{N_{syn}}$ at different *h* on the red observation point in (a). (d) Field-II wire-target simulation data at different *h*. (e) FWHM over imaging depth. (f) SNR difference between the TRUS-rSAF and TRUS-CON imaging over imaging depth.
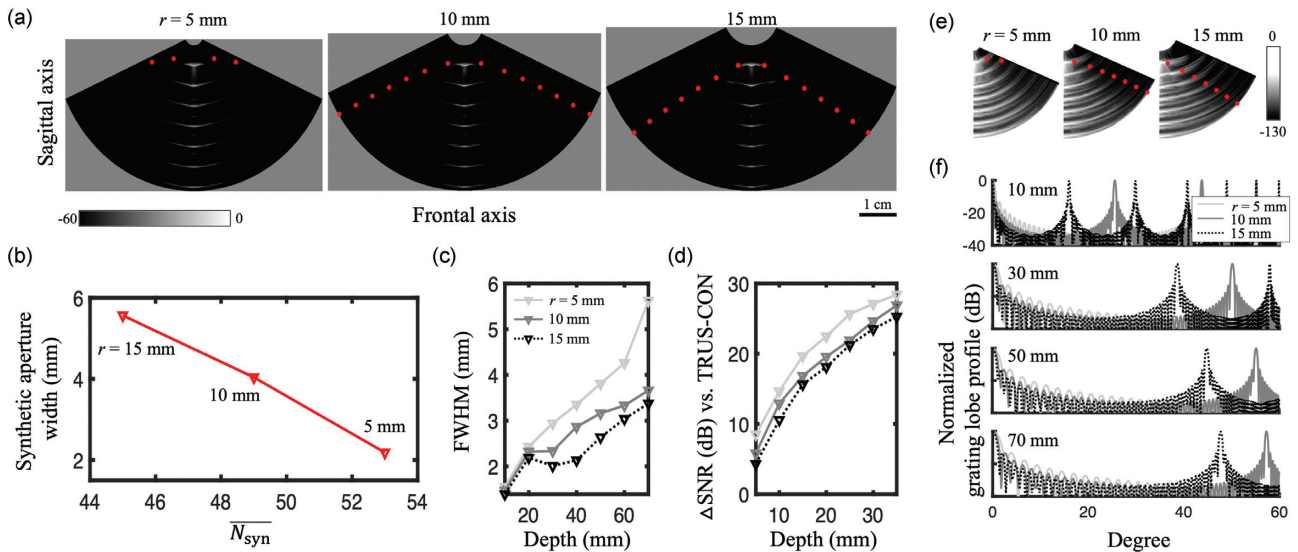

Figure 5: Critical parameter optimization on *r* impact on TRUS-rSAF imaging performance. (a) Field-II wire-target simulation data at different *r*. (b) Aperture size as a function of given $\overline{N_{syn}}$. (c) FWHM over imaging depth. (d) SNR difference between the TRUS-rSAF and TRUS-CON imaging over imaging depth. (e) TRUS-rSAF images with extended dynamic range. Red dots indicate the first grating lobe positions. (f) Theoretical grating lobe positions at 10, 30, 50, and 70 mm depths and at different *r*.

lobe artifacts at the near depth, i.e., 10 mm imaging depth. Grating lobes in the deeper depth will be suppressed, following the proportional relationship of the grating lobe positions to imaging depth z_f in Equation (13-2). Figure 6b shows the single-sided radial beam profiles of the center plane and the outmost plane. The

condition defines the corresponding Δθ at 0.1564°, producing the grating lobe positions at 40.96°. The corresponding B-mode image of the TRUS-GLR method successfully rejected grating lobe artifacts compared to the original design with Δθ at 0.4724°, as demonstrated in Fig. 6a. In addition, 2D cross-correlation coeffi-
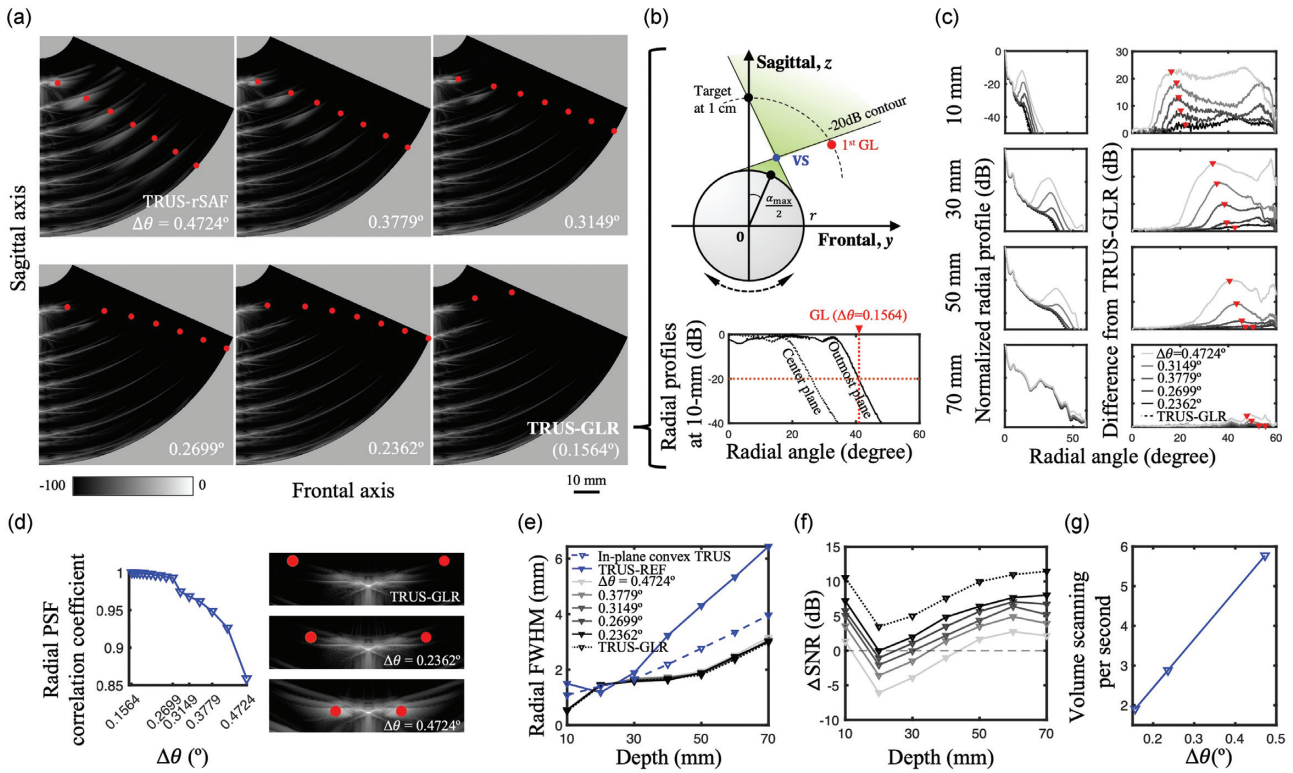
Figure 6: Global optimization of the TRUS-rSAF imaging performance. (a) Field-II wire-target simulation data at different $\Delta\theta$ (FOV = [0°, 66.14°]). Red dots indicate the first grating lobe positions. (b) Definition of grating-lobe-rejected TRUS (TRUS-GLR) imaging having the first grating lobe position out of outmost plane. (c) (Left-hand panel) Radial profiles at different depth. (Right-hand panel) Corresponding grating lobe intensity profiles subtracted by TRUS-GLR. Red marks indicate the first grating lobe positions. (d) 2D cross-correlation between the point-spread function (PSF) of TRUS-GLR and others at 10mm. (e) FWHM over imaging depth. (f) SNR difference between TRUS-rSAF and TRUS-REF over imaging depth. (g) Estimated volume rate at different $\Delta\theta$. (h) Field-II wire-target simulation data of TRUS-REF, TRUS-rSAF, and TRUS-GLR.

cients measured between PSFs of TRUS-GLR and other TRUS-rSAF images at 10 mm depth presented a noticeable drop from $\Delta\theta = 0.2699°$, suggesting grating lobe artifacts (Fig. 6d).

4.2. Signal-to-noise ratio

As discussed in the previous sections, the SNR of the TRUS-rSAF imaging is lowered by the diverging acoustic transmission but can be compensated by increasing $\overline{N_{syn}}$. Figure 6f presents the SNR difference between TRUS-rSAF and TRUS-REF imaging from the WTs over imaging depths. Note that the change of $\Delta\theta$ did not affect the spatial resolution by fixing α_{max} (i.e., $\theta_{max} = 30.23°$ with $\overline{N_{syn}}$: {65, 81, 97, 113, 129, 195} at $\Delta\theta$: {0.4724°, 0.3779°, 0.3149°, 0.2699°, 0.2362°, 0.1564°}).

Here we tested our design criterion to provide SNR comparable to that in the TRUS-REF imaging, by which the fundamental expectation in modern clinical TRUS diagnosis can be met. If we aim to have comparable or higher SNR at the entire depth range, the minimal $\Delta\theta$ should be 0.2362°. On the other hand, one may care more about deep tissue at 60 mm, given that the superficial region has less acoustic attenuation. In this case, the criterion is already achieved in the original TRUS-rSAF imaging specification of $\Delta\theta = 0.4724°$.

4.3. Volume scanning rate

Although reducing $\Delta\theta$ is effective in alleviating grating lobe artifacts and enhancing SNR, it presents a drawback in volume scanning rate. To illustrate, we first estimated a scanning time for the conventional imaging specifications effective for both TRUS-REF and TRUS-rSAF methods: 5 cm imaging depth; 5-plane-wave angle compounding in lateral dimension; 280 scanlines at $\Delta\theta$ of 0.4724°, constructing FOV over [−66.14°, 66.14°]; and θ_{max} of 30.23° (i.e., $\overline{N_{syn}}$ at 65). Note that mechanical and electrical transition times were not considered for a more straightforward presentation. The estimation starts from the round-trip time duration for the imaging depth (i.e., 6.49 μsec/cm acoustic propagation speed × 5 cm × 2 = 64.94 μsec) plus a redundant duration between radial planes (assumed to be 20 μsec), multiplied by the number of lateral compounding events (84.94 μsec × five compounding events = 424.70 μsec). These parameters lead to the total volume scanning time with the number of radial planes composing the volume (i.e., 424.70 μsec × 280 planes = 118.92 msec). In this case, a volume scanning rate is 8.41 volume/sec.

On the other hand, our SNR optimization of the TRUS-rSAF method required the minimal $\Delta\theta$ at 0.2362° to ultimately outperform the TRUS-REF method (Fig. 6f). In this case, the volume scanning time will be 237.82 msec, leading to a 50% reduction in the imaging rate (i.e., 4.20 volume/sec).

One may pursue extreme optimization for a complete rejection of grating lobe artifacts. The TRUS-GLR imaging suggests $\Delta\theta$ at 0.1564° for the effective rejection starting from near depth (>10 mm). In this case, the volume scanning times will be 359.18 msec, 302.04% longer than the original specifications (i.e., 118.92 msec). The corresponding volume scanning rate is 2.78 volume/sec.

Given the scenarios among multiple metrics (i.e., SNR, volume scanning rate, and grating lobe), users of the TRUS-rSAF imaging must prioritize their imaging specifications when determining $\Delta\theta$ in the TRUS-rSAF imaging.
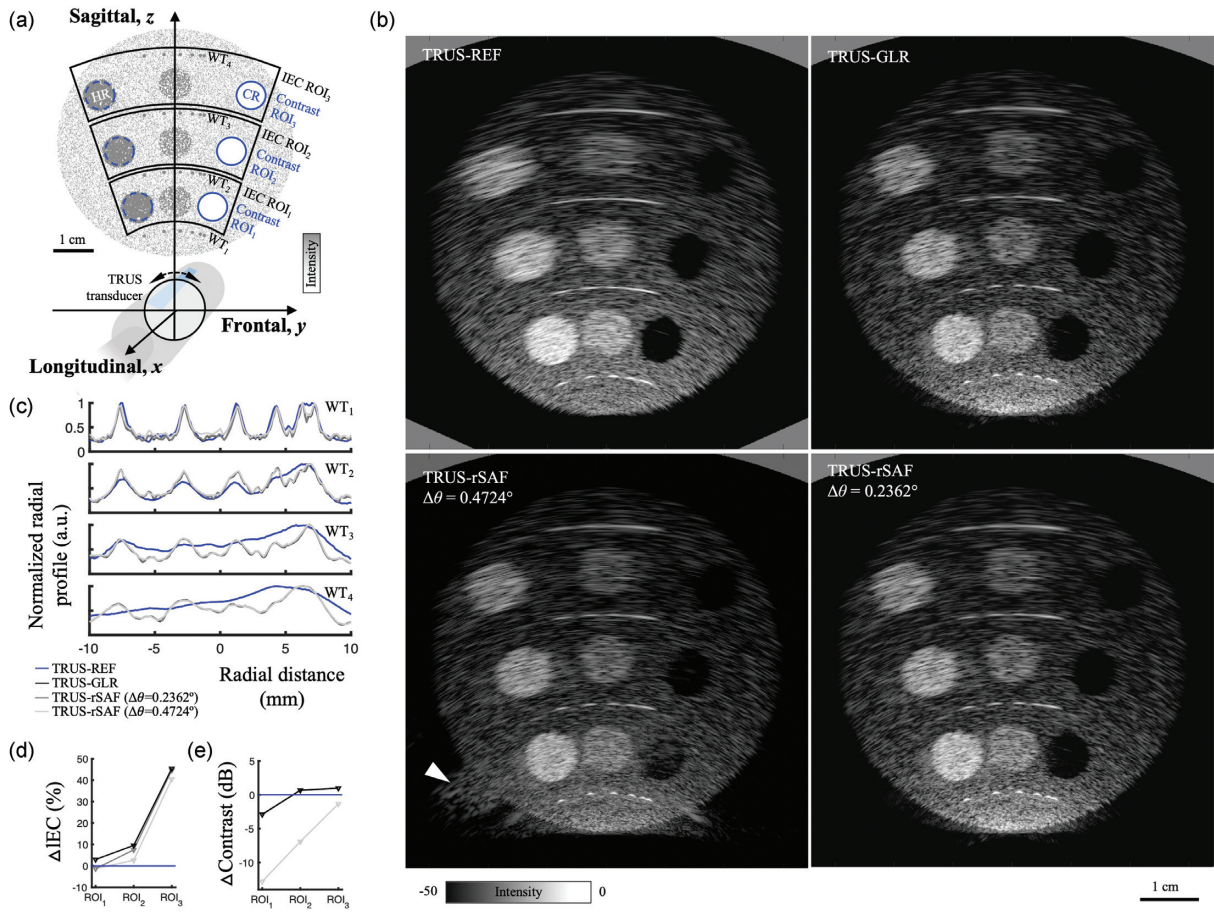
Figure 7: Evaluation of TRUS imaging simulation. (a) Geometrical illustration of the prostate-mimicking phantom. (b) TRUS images of simulated prostate imaging scenario. White dashed-line boxes represent the ROIs centered at 20, 35, and 50 mm, for measuring IEC. (c) Normalized 1D profiles of WT_1 (12.5 mm), WT_2 (27.5 mm), WT_3 (42.5 mm), and WT_4 (57.5 mm). (d) information entropy contrast values in the ROIs, (e) Fractional Contrast changes in decibel scale in the ROIs.

4.4. Tissue-mimicking simulation

A prostate tissue-mimicking Field-II simulation was performed to evaluate the functional performance of the TRUS-rSAF framework. Figure 7a shows the ground-truth field definition with WTs, HR, and CR. Figure 7b demonstrates the simulated B-mode images of TRUS-REF and TRUS-rSAF with different scanline intervals: $\Delta\theta = 0.4724°, 0.2362°$, and $0.1564°$ (TRUS-GLR). In visual assessment, apparent enhancement in spatial resolution was identified in the TRUS-GLR imaging. Relative improvements over the TRUS-REF imaging were evident in the deeper imaging depth. Figure 7c shows the 1D radial profiles of the WTs (WT_{1-4}), agreeing with the expectation from Fig. 6e – The TRUS-rSAF method well resolved < 3 mm distance in entire imaging depth regardless of $\Delta\theta$. Otherwise, the TRUS-REF imaging failed to resolve the 5 mm distance between targets from 50 mm depth. On the other hand, a significant amount of grating lobe artifacts was found in the TRUS-rSAF method when $\Delta\theta = 0.4724°$ as anticipated. The TRUS-rSAF with the optimized $\Delta\theta$ at 0.2362° showed the image quality comparable to that in the TRUS-GLR imaging with effective suppression of the grating lobe artifacts.

Quantitative evaluations were performed to validate the visual observations. The Contrast between the hyperechoic and hypoechoic targets in Fig. 7e indicated {30.08, 27.24, 25.12} dB in the TRUS-REF imaging at ROI_{1-3}. On the other hand, the TRUS-rSAF imaging showed {17.27, 20.32, 23.78} dB, {27.14, 27.92, 26.09}

dB, and {27.20, 27.92, 26.11} dB at {ROI_1, ROI_2, ROI_3} when $\Delta\theta = 0.4724°, 0.2362°$, and $0.1564°$, respectively. Notably, the TRUS-rSAF imaging at $\Delta\theta = 0.4724°$ presented a low Contrast value due to severe grating lobe artifacts. Otherwise, the TRUS-GLR ($\Delta\theta = 0.1564°$) and the optimized TRUS-rSAF imaging ($\Delta\theta = 0.2362°$) successfully suppressed the grating lobe artifacts, resulting in the higher Contrast values than the TRUS-REF imaging in ROI_{2-3}. The TRUS-REF imaging provided the higher Contrast value at ROI_1 due to the lower side lobe artifacts by tightly-focused transmittance/reception event at 20 mm, but the lower spatial resolution at other imaging depths should be reminded (Figs. 6e and 7c).

The IEC measurements at different depth range in Fig. 7d indicated the significant increase of visual information due to the TRUS-rSAF imaging. The IEC ROIs centered at {20, 35, 50} mm depths (i.e., ROI_1, ROI_2, and ROI_3) were {2.21, 0.74, 0.25}e^{-2} for the TRUS-REF method; {2.18, 0.76, 0.36}e^{-2}, {2.18, 0.80, 0.37}e^{-2}, and {2.28, 0.81, 0.37}e^{-2} for the TRUS-rSAF method when $\Delta\theta = 0.4724°$, 0.2362° and 0.1564°. The corresponding fractional improvements over the TRUS-REF imaging were {−1.32, −1.31, 2.99}% in ROI_1, {2.59, 7.47, 9.54}% in ROI_2, and {40.48, 44.62, 45.43}% in ROI_3 for $\Delta\theta = \{0.4724°, 0.2362°, 0.1564°\}$, respectively. The results indicate that the TRUS-rSAF and TRUS-REF imaging delivers comparable amount of visual information at 20 mm depth, but the TRUS-rSAF method clearly improves the image quality throughout the image.
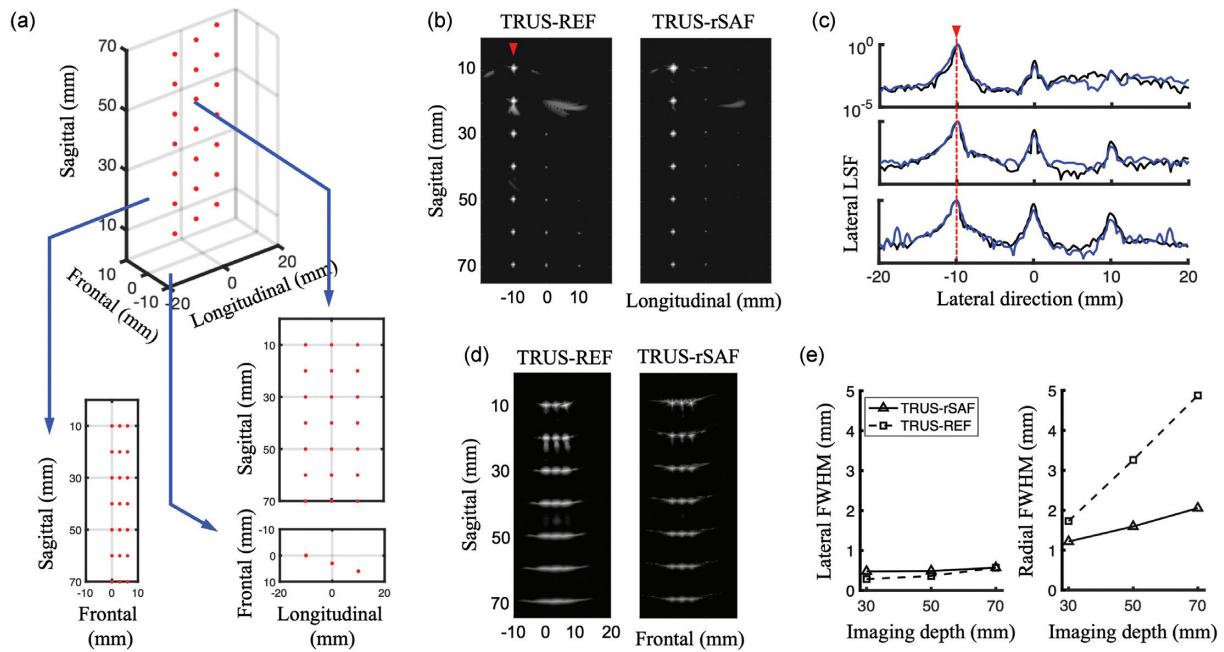
Figure 8: 3D imaging simulation. (a) WT locations in transverse-coronal-sagittal planes. (b) The TRUS-REF and TRUS-rSAF images in the transverse-sagittal dimension. (c) LSF over the sagittal dimension. Red arrows indicate the on-axis imaging plane at 0° scanning angle. LSF: Line-spread function. (d) The transverse-coronal planes. (e) Sagittal and coronal FWHMs.

4.5. 3D simulation

The analytical models of beamforming in two orthogonal dimensions (i.e., transverse and sagittal planes) are independent in defining theoretical spatial resolution and grating lobe positions for each dimension. Based on this, our simulation was performed in 2D. However, there should be crosstalk in practical imaging circumstances, depending on the given transducer design, target configuration, and spatial resolution. Herein, we evaluate the practical impact of the TRUS-rSAF method using optimized critical parameters on 3D imaging performance.

Volumetric imaging simulation was conducted with three columns and rows of point targets: {−10, 0, 10} mm in longitudinal direction and {0, 3, 6} mm in frontal direction (Fig. 8a). The point targets were repeated from 10 to 70 mm with a 10 mm interval on the sagittal axis. Each lateral scanning sequence consists of 31 plane-wave transmission and reception events using the entire lateral aperture of the TRUS array transducer with a range of steering from −15° to 15° at 1° interval. Depth-dependent signal processing techniques (e.g. apodization and dynamic aperture) were not applied to evaluate each method's raw TRUS imaging performance. Each lateral scanning sequence consists of multiple plane-wave transmittance and synthesis to generate a radial plane at each scanning angle. This sequence was repeated in the radial domain to scan the radial FOV from −65° to 65° with variable radial scanning interval $\Delta\theta$. Note that the VS in the elevation direction of the linear array was uniform in the lateral direction and did not affect the lateral beamforming process. In the TRUS-rSAF method, multiple radial planes are synthesized with appropriate compensation of synthetic time delay at each pixel position. The TRUS-REF method only took a single radial plane obtained at the target scanning angle. The envelope of the volumetric RF data is detected by bandpass-filtered Hilbert transform (3.9–9.1 MHz), and a digital scan converter produces 3D TRUS image data. The target radial plane was selected at 0° scanning angle. The trans-

verse plane was presented with the maximum intensity projection map in the longitudinal direction. Our quantitative metrics were how much off-axis point target intensities could be suppressed in the sagittal plane and FWHMs in the transverse plane.

Figure 8b and d show sagittal and transverse imaging planes reconstructed by the TRUS-REF and TRUS-rSAF methods. In the sagittal plane, the substantial off-axis intensity from 0 mm and 10 mm lateral columns were identified in the TRUS-REF image primarily due to limited radial resolution, as presented in Fig. 6e. The TRUS-rSAF method also showed off-axis interferences but less intensity in deep tissue and alleviated lateral grating lobe artifacts due to radial synthesis. Figure 8c presents lateral beam profiles at {30, 50, 70} mm imaging depths. Compared to those at on-axis intensities at −10 mm lateral column, the TRUS-rSAF method showed off-axis target of {1.78, 7.66, 16.26}% at 0 mm lateral column and {0.70, 0.99, 2.82}% at 10 mm lateral column in {30, 50, 70} mm imaging depths, respectively. On the other hand, the TRUS-REF method showed substantial interferences from the off-axis targets: {4.94, 20.06, 51.75}% and {0.79, 2.42, 9.22}% at {30, 50, 70} mm imaging depths, respectively, of those at on-axis intensities at −10 mm longitudinal column. In shallower imaging depths at 10 and 20 mm, higher off-axis intensities in the TRUS-rSAF method were identified, but there was another advantage of reducing lateral grating lobe artifacts with the radial synthesis in the depth range. Figure 8e shows the spatial resolution measured in sagittal and transverse planes of the TRUS-REF and TRUS-rSAF images. Lateral FWHM at 0° scanning angle were {0.47, 0.48, 0.57} mm and {0.30, 0.36, 0.57} mm in the TRUS-rSAF and TRUS-REF methods at {30, 50, 70} mm imaging depths, respectively. The TRUS-rSAF method showed slightly broadened FWHM, presumably due to the changes in TRUS array design, but both methods successfully provided spatial resolution below 0.5 mm. Any other combinations of the critical design parameters (i.e., d_{VS}, h, and r) will likely produce a lateral FWHM between them, as the TRUS-REF

and TRUS-rSAF methods represent highly diversified cases. In the transverse plane at the 0 mm frontal position, the same results were found as already presented in Fig. 6, showing significant improvements in radial FWHM by the TRUS-rSAF method than those by the TRUS-REF method with the fractional improvement of {25.61, 51.23, 57.73}% at {30, 50, 70} mm, respectively.

5. Conclusions

This paper demonstrated the novel analytical design strategy and optimization workflow of the TRUS-rSAF method to secure unprecedented volumetric imaging quality. The closed-form analytical model identified the critical parameters (i.e., d_{VS}, h, and r), affecting the TRUS-rSAF imaging spatial resolution and grating lobe positions, as theorized in Equations (13-1) and (13-2). Here, adding lens focusing property to the analytical solution will be a limiting factor of the integral in the α domain in our analytical development, narrowing the radial synthetic window. However, we wanted the analytical description of the TRUS-rSAF method to be a theoretical platform to investigate different SAF scenarios. This objective was achieved by assuming omni-directional acoustic propagation while having $p_s(\alpha)$ as a variable synthetic window function to investigate different transmit schemes on a user's own. For example, one may try to build a TRUS array with minimal h to maximize the acoustic divergence (i.e., $-90°$ to $90°$), leading to the broadest possible radial synthetic window. However, there would be a critical drawback of reduced acoustic intensity, which will lower SNR in deep imaging depth. Moreover, the fabrication of such a TRUS array transducer will be highly challenging. The VS approach with the elevation focusing lens secures translational practicality, providing wide-enough $p_s(\alpha)$ and transmit power in deep tissue, and $p_s(\alpha)$ is decided by testing a different number of radial planes for synthesis to minimize the FWHM.

The perspectives obtained from the analytical approach led to the solid optimization workflow, resulting in significantly superior spatial resolution compared to the volumetric TRUS-REF imaging. The analytical solution derives spatial resolution and grating lobe positions by observing continuous-wave interactions from different transmit source positions. One might be concerned about the monochromatic analysis at the center frequency of the TRUS array transducer (6.5 MHz), which will make it challenging to quantify its correlation to practical simulation results that consider pulsed acoustic transmission with broad bandwidth. However, our simulation showed "qualitative" agreement by the Equation (13-1), providing spatial resolution proportional to r and α_{max} and accurate localization of the first grating lobe positions, enough to be a design framework to optimize the TRUS imaging performance. Our spatial resolution-oriented optimization let the TRUS-rSAF method even outperform the in-plane micro-convex TRUS imaging of a transverse plane (Fig. 6), which is a promising advance to innovate the pelvic diagnosis.

On the other hand, the impacts of the optimization on the signal sensitivity and interferences were balanced for practical image quality enhancement. From the analytical model of the TRUS-rSAF imaging, we propose an essential role of the $\Delta\theta$ parameter to define the SNR and the first grating lobe positions. Specific optimization criteria were to sustain the SNR level of the TRUS-REF imaging while completely removing the grating lobe artifacts. Moreover, a prostate mimicking phantom was simulated to evaluate the clinical effectiveness of the optimized TRUS-rSAF method. In addition to the higher spatial resolution compared to the TRUS-REF method, TRUS-rSAF imaging delivered more image information than the TRUS-REF method with higher Contrast and IEC

metrics. On the other hand, a clinically effective volume scanning rate is implementable at the user's preference on imaging quality when compared to a clinical 3D TRUS imaging: 2–8 Hz in Fig. 6g vs. 3–6 Hz (Fenster & Downey, 1999; Fenster et al., 2011).

In terms of computing time, our data processing time for a single volume reconstruction by the TRUS-REF and TRUS-rSAF methods took 12.4 and 18.5 hours under single-core processing with a personal laptop (2.6GHz Intel Core i7 8850H, 16GB RAM, MATLAB 2020b). However, they are just technical numbers and do not reflect what should be expected in a clinical device. The SAF method has been widely used in clinical real-time US imaging platforms and has been marginally handled by modern GPU-accelerated computing units and efficient beamformer architectures (Park et al., 2010; Yiu et al., 2011; Jensen et al., 2013; Stuart et al., 2021). There is no technological hurdle to secure a clinically appropriate level of temporal resolution.

3D imaging simulation also brought attention to the benefits of the TRUS-rSAF method to obtain lower off-axis interferences and lateral grating lobe artifacts than those in the TRUS-REF method. Experimental validation is limited at this research stage, as our TRUS-rSAF method necessitates the extensive revision of the current clinical TRUS array transducer, which is currently not accessible to us. We performed a limited phantom study evaluating the effect of r changes using a clinical TRUS array (BPL9-5/55) maneuvered by two translational stages and one rotational stage. We achieved a high positive correlation between simulation and real-world data (refer to the Supplementary Information page). However, regardless of the encouraging results, an implication of the data is still insufficient to present the full benefits of our TRUS-rSAF method. Therefore, we will present complete experimental evidence of the TRUS-rSAF imaging enhancements in our following study.

We plan following further works to elaborate the TRUS-rSAF imaging framework for tangible clinical innovations:

(i) A customized TRUS transducer with the optimized parameters will be implemented, in which the full potential of the proposed analytical design strategy can be used for better imaging quality. In this article, our analytical development was focused on understanding which imaging and transducer design parameters affect the volumetric imaging quality metrics. This development further suggests a vital direction to pursue the mechanical evolution of the TRUS array transducer, which is under translational development in our group. An effective radial scanning configuration will be embedded to provide the optimal r and $\Delta\theta$ for high spatial resolution, SNR, grating lobe suppression, volume scanning rate, and patient comfort. The developed system will be first evaluated in practical circumstances by imaging large animal models and human subjects, leading to clinical study.

(ii) We will also identify the efficacy of the analytical model to describe the resource-limited volumetric imaging circumstance. For example, the radial scanning accuracy in locating individual planes depends on the performance of the rotational actuator. The framework necessitates its sophisticated integration to a TRUS transducer, which will increase the overall cost. We will develop an efficient TRUS imaging system that can provide a robust imaging performance using a low-cost actuator or an external angle tracker. The analytical model will be evolved to reflect the uncertainty of the low-accuracy angle tracking. In detail, the scanning errors of various tracking solutions will be

stochastically modeled with the revised Equation (2). The mathematical derivation will produce the resultant shift of the synthesized beam profile modified from Equation (7). This analytical approach will again result in a practical strategy to alleviate the volumetric imaging accuracy. The successful development of the low-cost volumetric TRUS imaging strategy will synergize with our ultra-compact US imaging solutions (Kim *et al.*, 2012; Ahn *et al.*, 2015; Kang *et al.*, 2016).

(iii) Moreover, novel algorithms to reject grating lobe artifacts can be developed by examining Equation (13-2) during an imaging session to separate different signal features of the signal and interference components. Such signal processing may help further enhance temporal resolution with alleviated $\Delta\theta$ restriction to reduce grating lobe artifacts.

(iv) We presented our analytical description of the TRUS-rSAF method in Cartesian coordination to secure a closed-form but deriving in cylindrical coordination may provide a way to further simplify the outcome. Moreover, the Fresnel approximation applied to Equation (6) may bring a validity issue. In the TRUS-rSAF imaging scenario, the radial synthetic window gives a range of y positions of the TRUS array, i.e., $r \sin(\theta_{max})$. Suppose $r = 15$ mm and $\theta_{max} = 30°$, the y position of the TRUS array would be at 7.5 mm. It is valid for deep imaging depth but may gradually lose its validity as the imaging depth is close to the TRUS array. We will keep pursuing a more generalized analytical model of the TRUS-rSAF method.

(v) The efficacy of the rSAF technique can extend beyond the TRUS imaging. There are many novel volume scanning approaches with rotational scanning (Kang *et al.*, 2021; Xu *et al.*, 2022). Our analytical solution presented in this article may help to improve their imaging performance to an unprecedented level.

We will further generalize our analytical description of the radial scanning configuration toward enabling a synthetic tracked aperture ultrasound imaging framework, in which a volumetric synthetic window is arbitrarily changed by a tracked robotic arm (Zhang *et al.*, 2016). The analytical model of the TRUS-rSAF imaging may play an essential part in describing the radial synthesis of the arbitrary planes. Such a comprehensive analytical approach to enable an arbitrary SAF in translational and rotational dimensions will open a new opportunity to develop more reliable robot-assisted US imaging diagnostics.

We also envision the application of the developed TRUS-rSAF method beyond conventional US diagnostics. Photoacoustic (PA) imaging is an emerging modality that can provide rich optical contrast at high spatiotemporal resolution in deep biological tissue (Wang, 2009; Wang & Hu, 2012). Thanks to its hybrid mechanism between optics and acoustics, novel clinical and scientific applications have been investigated extensively (Kang *et al.*, 2015, 2017, 2019, 2020). Our group recently presented a molecular PA imaging of prostate-specific membrane antigen (PSMA) which is overexpressed in aggressive tumors (Zhang *et al.*, 2018; Lesniak *et al.*, 2021). We will further merge the analytical approach to optimizing TRUS-rSAF imaging for localizing PSMA expression at high spatiotemporal and contrast resolution, which will secure higher clinical sensitivity and specificity.

Authors' contributions statement

Acknowledgments

Conflict of interest statement

None declared.

References

Ahn, S., Kang, J., Kim, P., Lee, G., Jeong, E., Jung, W., Park, M., & Song, T.-k. (2015). Smartphone-Based Portable Ultrasound Imaging System: Prototype Implementation and Evaluation. In *Proceedings of the 2015 IEEE International Ultrasonics Symposium (IUS)* (pp. 1–4). IEEE. https://doi.org/10.1109/ultsym.2015.0517.

Andresen, H., Nikolov, S. I., Pedersen, M. M., Buckton, D., & Jensen, J. A. (2010). Three-dimensional synthetic aperture focusing using a rocking convex array transducer. *IEEE Transactions on Ultrasonics, Ferroelectrics and Frequency Control*, **57**(5), 1051–1063. https://doi.org/10.1109/tuffc.2010.1517.

Andresen, H., Nikolov, S. I., Jensen, J. A., Andresen, H., Nikolov, S. I., & Jensen, J. A. (2011). Synthetic aperture focusing for a single-element transducer undergoing helical motion. *IEEE Transactions on Ultrasonics, Ferroelectrics and Frequency Control*, **58**(5), 935–943. https://doi.org/10.1109/tuffc.2011.1894.

Bae, M. H., & Jeong, M. K. (2000). A study of synthetic-aperture imaging with virtual source elements in B-mode ultrasound imaging systems. *IEEE Transactions on Ultrasonics, Ferroelectrics, and Frequency Control*, **47**(6), 1510–1519. https://doi.org/10.1109/58.883540.

Bae, S., Kim, P., & Song, T. (2018). Ultrasonic sector imaging using plane wave synthetic focusing with a convex array transducer. *The Journal of the Acoustical Society of America*, **144**(5), 2627–2644. https://doi.org/10.1121/1.5065391.

Bottenus, N., Long, W., Zhang, H. K., Jakovljevic, M., Bradway, D. P., Boctor, E. M., & Trahey, G. E. (2016a). Feasibility of swept synthetic aperture ultrasound imaging. *IEEE Transactions on Medical Imaging*, **35**(7), 1676–1685. https://doi.org/10.1109/tmi.2016.2524992.

Chang, J. H., & Song, T.-K. (2011). A new synthetic aperture focusing method to suppress the diffraction of ultrasound. *IEEE Transactions on Ultrasonics, Ferroelectrics and Frequency Control*, **58**(2), 327–337. https://doi.org/10.1109/tuffc.2011.1810.

Cobbold, R. S. C. (2006). Section 3.4.1. Fresnel and Fraunhofer approximations. In *Foundations of biomedical ultrasound* (p. 155). Oxford University Press.

Coleman, J., Nascimento, R., & Solomon, S. B. (2007). Advances in imaging for urologic procedures. *Nature Clinical Practice Urology*, **4**(9), 498–504. https://doi.org/10.1038/ncpuro0883.

Fenster, A., & Downey, D. B. (1999). Three-dimensional ultrasound imaging of the prostate. In *Proceedings of the SPIE Conference Series Volume 3659, Medical Imaging 1999: Physics of Medical Imaging*(pp. 2–11). SPIE. https://doi.org/10.1117/12.349496.

Fenster, A., & Downey, D. B. (2000). Three-dimensional ultrasound imaging. *Annual Review of Biomedical Engineering*, **2**(1), 457–475. https://doi.org/10.1146/annurev.bioeng.2.1.457.

Fenster, A., Parraga, G., & Bax, J. (2011). Three-dimensional ultrasound scanning. *Interface Focus*, **1**(4), 503–519. https://doi.org/10.1098/rsfs.2011.0019.

Frazier, C. H., & O'Brien, W. D. (1998). Synthetic aperture techniques with a virtual source element. *IEEE Transactions on Ultrasonics, Ferroelectrics, and Frequency Control*, **45**(1), 196–207. https://doi.org/10.1109/58.646925.

Hu, Q., Xie, Z. X., Wang, Z. F., & Liu, Y. H. (2008). Constructing NR-IQA function based on product of information entropy and contrast. *2008 International Symposium on Information Science and Engineering*, **2**, 548–550. https://doi.org/10.1109/isise.2008.93.

Jensen, J. A. (1996). Field: A program for simulating ultrasound systems. *Medical & Biological Engineering & Computing*, **34**, 351–352.

Jensen, J. A., Nikolov, S. I., Gammelmark, K. L., & Pedersen, M. H. (2006). Synthetic aperture ultrasound imaging. *Ultrasonics*, **44**, e5–e15. https://doi.org/10.1016/j.ultras.2006.07.017.

Jensen, J. A., Holten-Lund, H., Nilsson, R. T., Hansen, M., Larsen, U. D., Domsten, R. P., Tomov, B. G., Stuart, M. B., Nikolov, S. I., Pihl, M. J., Du, Y., Rasmussen, J. H., & Rasmussen, M. F. (2013). SARUS: A synthetic aperture real-time ultrasound system. *IEEE Transactions on Ultrasonics, Ferroelectrics, and Frequency Control*, **60**(9), 1838–1852. https://doi.org/10.1109/tuffc.2013.2770.

Jensen, J. A., & Svendsen, N. B. (1992). Calculation of pressure fields from arbitrarily shaped, apodized, and excited ultrasound transducers. *IEEE Transactions on Ultrasonics, Ferroelectrics and Frequency Control*, **39**(2), 262–267. https://doi.org/10.1109/58.139123.

Ju, H., Kang, J., Song, I., & Yoo, Y. (2015). A new multi-planar reconstruction method using voxel based beamforming for 3D ultrasound imaging. In *Proceedings of the SPIE Conference Series Volume 9412, Medical Imaging 2015: Physics of Medical Imaging*(p. 94124P). SPIE. https://doi.org/10.1117/12.2080935.

Kang, J., Kim, E., Kim, G. R., Yoon, C., Song, T., & Chang, J. H. (2015). Photoacoustic imaging of breast microcalcifications: A validation study with 3-dimensional ex vivo data and spectrophotometric measurement. *Journal of Biophotonics*, **8**(1–2), 71–80. https://doi.org/10.1002/jbio.201300100.

Kang, J., Yoon, C., Lee, J., Kye, S.-B., Lee, Y., Chang, J. H., Kim, G.-D., Yoo, Y., & Song, T.-K. (2016). A system-on-chip solution for point-of-care ultrasound imaging systems: Architecture and ASIC implementation. *IEEE Transactions on Biomedical Circuits and Systems*, **10**(2), 412–423. https://doi.org/10.1109/tbcas.2015.2431272.

Kang, J., Chang, J. H., Kim, S. M., Lee, H. J., Kim, H., Wilson, B. C., & Song, T.-K. (2017). Real-time sentinel lymph node biopsy guidance using combined ultrasound, photoacoustic, fluorescence imaging: In vivo proof-of-principle and validation with nodal obstruction. *Scientific Reports*, **7**(1), 45008. https://doi.org/10.1038/srep45008.

Kang, J., Zhang, H. K., Kadam, S. D., Fedorko, J., Valentine, H., Malla, A. P., Yan, P., Harraz, M. M., Kang, J. U., Rahmim, A., Gjedde, A., Loew, L. M., Wong, D. F., & Boctor, E. M. (2019). Transcranial recording of electrophysiological neural activity in the rodent brain in vivo using functional photoacoustic imaging of near-infrared voltage-sensitive dye. *Frontiers in Neuroscience*, **13**, 579. https://doi.org/10.3389/fnins.2019.00579.

Kang, J., Kadam, S. D., Elmore, J. S., Sullivan, B. J., Valentine, H., Malla, A. P., Harraz, M. M., Rahmim, A., Kang, J. U., Loew, L. M., Baumann, M.

H., Grace, A. A., Gjedde, A., Boctor, E. M., & Wong, D. F. (2020). Transcranial photoacoustic imaging of NMDA-evoked focal circuit dynamics in the rat hippocampus. *Journal of Neural Engineering*, **17**(2), 025001. https://doi.org/10.1088/1741-2552/ab78ca.

Kang, S., Lee, J., & Chang, J. H. (2021). Effectiveness of synthetic aperture focusing and coherence factor weighting for intravascular ultrasound imaging. *Ultrasonics*, **113**, 106364. https://doi.org/10.1016/j.ultras.2021.106364.

Kim, G.-D., Yoon, C., Kye, S.-B., Lee, Y., Kang, J., Yoo, Y., & Song, T. K. (2012). A single FPGA-based portable ultrasound imaging system for point-of-care applications. *IEEE Transactions on Ultrasonics, Ferroelectrics and Frequency Control*, **59**(7), 1386–1394. https://doi.org/10.1109/tuffc.2012.2339.

Kim, C., Yoon, C., Park, J.-H., Lee, Y., Kim, W. H., Chang, J. M., Choi, B. I., Song, T.-K., & Yoo, Y. M. (2013). Evaluation of ultrasound synthetic aperture imaging using bidirectional pixel-based focusing: Preliminary phantom and in vivo breast study. *IEEE Transactions on Biomedical Engineering*, **60**(10), 2716–2724. https://doi.org/10.1109/tbme.2013.2263310.

Kim, J. S., Lee, J. G., Choi, J. H., Han, B. H., Yoon, S. L., Jung, H., Song, T. K., & Lee, J. Y. (2019). A universal ultrasound diagnostic system developed to support urology and coloproctological applications. *Biomedical Engineering Letters*, **9**(1), 119–125. https://doi.org/10.1007/s13534-018-0088-x.

Kortbek, J., Jensen, Jø. A., & Gammelmark, K. Lø. (2008). Synthetic aperture sequential beamforming. In *Proceedings of the 2008 IEEE Ultrasonics Symposium*(pp. 966–969). IEEE. https://doi.org/10.1109/ultsym.2008.0233.

Lee, Y., Lee, W. Y., Lim, C.-E., Chang, J. H., Song, T. K., & Yoo, Y. (2012). Compounded direct pixel beamforming for medical ultrasound imaging. *IEEE Transactions on Ultrasonics, Ferroelectrics and Frequency Control*, **59**(3), 573–582. https://doi.org/10.1109/tuffc.2012.2231.

Lesniak, W. G., Wu, Y., Kang, J., Boinapally, S., Banerjee, S. R., Lisok, A., Jablonska, A., Boctor, E. M., & Pomper, M. G. (2021). Dual contrast agents for fluorescence and photoacoustic imaging: Evaluation in a murine model of prostate cancer. *Nanoscale*, **13**(20), 9217–9228. https://doi.org/10.1039/d1nr00669j.

Lucas, T., Quidu, I., Bridal, S. L., & Gateau, J. (2021). High-contrast and -resolution 3-D ultrasonography with a clinical linear transducer array scanned in a rotate-translate geometry. *Applied Sciences*, **11**(2), 493. https://doi.org/10.3390/app11020493.

Nikolov, S. I., & Jensen, J. A. (2000). 3D synthetic aperture imaging using a virtual source element in the elevation plane. In *2000 IEEE Ultrasonics Symposium. Proceedings. An International Symposium (Cat. No.00CH37121)*(pp. 1743–1747). IEEE. https://doi.org/10.1109/ultsym.2000.921659.

Park, J.-H., Yoon, C., Chang, J. H., Yoo, Y., & Song, T. K. (2010). A real-time synthetic aperture beamformer for medical ultrasound imaging. In *Proceedings of the 2010 IEEE International Ultrasonics Symposium*(pp. 1992–1995). IEEE. https://doi.org/10.1109/ultsym.2010.5935734.

Pedersen, M. H., Gammelmark, K. L., & Jensen, J. A. (2007a). In-vivo evaluation of convex array synthetic aperture imaging. *Ultrasound in Medicine & Biology*, **33**(1), 37–47. https://doi.org/10.1016/j.ultrasmedbio.2006.07.041.

Perrin, P. (1992). Transrectal ultrasound for the diagnosis and staging of prostate cancer. *Current Opinion in Urology*, **2**(5), 344–347. https://doi.org/10.1097/00042307-199210000-00005.

Stuart, M. B., Jensen, P. M., Olsen, J. T. R., Kristensen, A. B., Schou, M., Dammann, B., Sørensen, H. H. B., & Jensen, J. A. (2021). Real-time volumetric synthetic aperture software beamforming of row–column probe data. *IEEE Transactions on Ultrasonics, Ferroelectrics,*

and Frequency Control, **68**(8), 2608–2618. https://doi.org/10.1109/tuffc.2021.3071810.

Trabulsi, E. J., Sackett, D., Gomella, L. G., & Halpern, E. J. (2010). Enhanced transrectal ultrasound modalities in the diagnosis of prostate cancer. *Urology*, **76**(5), 1025–1033. https://doi.org/10.1016/j.urology.2010.05.022.

Tsui, P. H., Chen, C. K., Kuo, W. H., Chang, K. J., Fang, J., Ma, H. Y., & Chou, D. (2017). Small-window parametric imaging based on information entropy for ultrasound tissue characterization. *Scientific Reports*, **7**(1), 41004. https://doi.org/10.1038/srep41004.

Wang, L. V. (2009). Multiscale photoacoustic microscopy and computed tomography. *Nature Photonics*, **3**(9), 503–509. https://doi.org/10.1038/nphoton.2009.157.

Wang, L. V., & Hu, S. (2012). Photoacoustic tomography: In vivo imaging from organelles to organs. *Science*, **335**(6075), 1458–1462. https://doi.org/10.1126/science.1216210.

Xu, K., Jiang, B., Moghekar, A., Kazanzides, P., & Boctor, E. (2022). AutoInFocus, a new paradigm for ultrasound-guided spine intervention: A multi-platform validation study. *International Journal of Computer Assisted Radiology and Surgery*, **17**, 911–920. https://doi.org/10.1007/s11548-022-02583-6.

Yiu, B. Y. S., Tsang, I. K. H., & Yu, A. C. H. (2011). GPU-based beamformer: Fast realization of plane wave compounding and synthetic aperture imaging. *IEEE Transactions on Ultrasonics, Ferroelectrics, and Frequency Control*, **58**(8), 1698–1705. https://doi.org/10.1109/tuffc.2011.1999.

Zhang, H. K., Aalamifar, F., Trahey, G. E., & Boctor, E. M. (2016). In vivo visualization of robotically implemented synthetic tracked aperture ultrasound (STRATUS) imaging system using curvilinear array. In *Proceedings of the SPIE Conference Series Volume 9790, Medical Imaging 2016: Ultrasonic Imaging and Tomography*(p. 97901X). SPIE. https://doi.org/10.1117/12.2217278.

Zhang, H. K., Chen, Y., Kang, J., Lisok, A., Minn, I., Pomper, M. G., & Boctor, E. M. (2018). Prostate-specific membrane antigen-targeted photoacoustic imaging of prostate cancer in vivo. *Journal of Biophotonics*, **11**(9), e201800021. https://doi.org/10.1002/jbio.201800021.